

Optimizing disorder with machine learning to harness synchronization

Jun-Yin Huang,¹ Zheng-Meng Zhai,¹ Li-Li Ye,¹ Vassilios Kovanis,^{2,3} and Ying-Cheng Lai^{1,4,*}

¹*School of Electrical, Computer and Energy Engineering,
Arizona State University, Tempe, AZ 85287, USA*

²*Bradley Department of Electrical and Computer Engineering,
Virginia Tech Research Center, 900 N. Glebe Rd, Arlington, VA 22203, USA*

³*Virginia Tech National Security Institute, Research Center,
900 North Glebe Rd., Arlington, VA 22203, USA*

⁴*Department of Physics, Arizona State University, Tempe, Arizona 85287, USA*

(Dated: April 15, 2025)

Disorder is often considered detrimental to coherence. However, under specific conditions, it can enhance synchronization. We develop a machine-learning framework to design optimal disorder configurations that maximize phase synchronization. In particular, utilizing the system of coupled nonlinear pendulums with disorder and noise, we train a feedforward neural network (FNN), with the disorder parameters as input, to predict the Shannon entropy index that quantifies the phase synchronization strength. The trained FNN model is then deployed to search for the optimal disorder configurations in the high-dimensional space of the disorder parameters, providing a computationally efficient replacement of the stochastic differential equation solvers. Our results demonstrate that the FNN is capable of accurately predicting synchronization and facilitates an efficient inverse design solution to optimizing and enhancing synchronization.

I. INTRODUCTION

Coupled nonlinear oscillators arise commonly in physical, biological and engineering systems, where the universal collective behavior of synchronization is of interest and has been extensively investigated [1]. If the individual oscillators are identical, complete synchronization can occur, where the dynamical evolution of all oscillators approaches a single oscillatory solution if the mutual couplings among the oscillators are sufficiently strong. This idealized setting allows the stability of the synchronous solution to be mathematically analyzed [2–4]. In network science, earlier work demonstrated that networks with a complex topology, in particular small-world networks, are easier to be synchronized than regular networks [5–8], based on the intuition that the network diameter determines the “communication” capability of the network [9] and that the communication can be more readily achieved on networks with a smaller diameter, rendering them more synchronizable. This result holds for homogeneous networks with a uniform, e.g., Poisson, degree distribution. However, for heterogeneous networks with a power-law degree distribution such as scale-free networks, the opposite may hold: as the network become more heterogeneous, the average network diameter is reduced but synchronization becomes more difficult to achieve, which can be heuristically understood by the heterogeneous distribution of the betweenness centrality measure [10, 11]. A mathematical framework to analyze synchronization in complex networks is simultaneous block diagonalization of the Laplacian matrix, but it may fail when applying to complete and cluster synchronization of random networks [12]. Quite recently, the

notion of network syncreactivity was proposed to understand the transient behavior toward synchronization and the efficiency of synchronization dynamics [13]. Strictly speaking, all these results hold only for networks of coupled identical nonlinear oscillators.

In networked systems arising from the real world, the oscillators are seldom identical. Intuitively, when the oscillators are nonidentical, synchronization can break down, as demonstrated theoretically and experimentally [14]. For such systems, it becomes challenging to define the synchronization manifold, but if the degree of heterogeneity in the individual oscillator dynamics is not too severe, a generalized synchronization manifold can still be mathematically constructed [15]. For example, localized synchronization in two coupled nonidentical semiconductor lasers was observed [16], where the two lasers exhibit quite different amplitudes of oscillations. In a general sense, a set of nonidentical oscillators can be viewed as a set of identical oscillators with random disorders applied to the individual oscillators. The disorders can manifest themselves as some external perturbations to the oscillators or random variations in the system parameters. It was discovered earlier that random disorders can be exploited to modulate or tame spatiotemporal chaos [17]. It was also found in an array of coupled, externally driven, chaotic mechanical oscillators that random phases in the driving forces can result in regular dynamical behaviors, in spite of the individual oscillators being chaotic when uncoupled [18]. A remarkable phenomenon was that random parameter heterogeneity among the oscillators can counter intuitively promote synchronization [19, 20]. Even more surprisingly, for coupled chaotic oscillators, there are parameter regimes where oscillator heterogeneity can lead to synchronization for conditions under which identical oscillators cannot [21]. Recently, synchronization in networked

* Ying-Cheng.Lai@asu.edu

systems with large parameter mismatches was studied in terms of the stability of the synchronous state and the transition to synchronization [22].

Exploiting physically feasible quantities such as disorders and time delays to achieve synchronization provides a way to achieve desired synchronization-based system performance, such as enhancing the collective coherence of lasers for applications [23–27]. For example, when lasers are phase-locked, they can produce a coherent, high-power beam that can be focused into a single-lobe far-field pattern [28], and this has applications in photonics [29]. Recently, the possibility of using disorder to overcome disorder to achieve frequency and phase synchronization of diode laser arrays has been numerically demonstrated and theoretically analyzed [30]. The previous results on the beneficial role of random disorders in synchronization notwithstanding, an open question remains: Given a system of coupled nonlinear oscillators, how to find the optimal configurations of disorders that maximize synchronization? In general, the dimension of the space of the parameters characterizing the disorders can be exceedingly high, defying any brute-force type of search for the optimal parameters. In this paper, we demonstrate that machine learning provides a viable solution.

To be concrete, we consider a coupled array of forced and damped nonlinear oscillators [17, 18, 31], derived from the Frenkel-Kontorova model [32]. To account for environmental factors such as thermal fluctuations, external vibrations, and mechanical imperfections, we add Gaussian noise to the system. The driving is assumed to be sinusoidal and the random disorders are manifested in the phase of the driving. That is, the phase of the driving on each oscillator is a random variable taken from certain probability distribution [18]. Given a disorder configuration, it is necessary to solve a set of coupled stochastic differential equations to determine if synchronization has been achieved. The key challenge in finding an optimal disorder configuration lies in the computational complexity: systematically searching through the continuous parameter space of the disorders is simply computationally prohibitive. We address this challenge by employing a feedforward neural network (FNN) to replace the stochastic differential equation solver, leading to a significant reduction in the computational cost. In particular, if the system has N oscillators and each oscillator has one disorder parameter that can be externally adjusted, the dimension of the disorder parameter space is N . We first employ random sampling in the N -dimensional parameter space to gather training and testing data by directly solving the stochastic differential equations. The input data to the neural network is thus an N -dimensional vector comprising the disorder phases, while the output is a measure characterizing the degree of synchronization, e.g., the Shannon entropy index [33]. We then demonstrate that, once trained, the neural network is capable of searching through the entire disorder parameter space, including previously un-

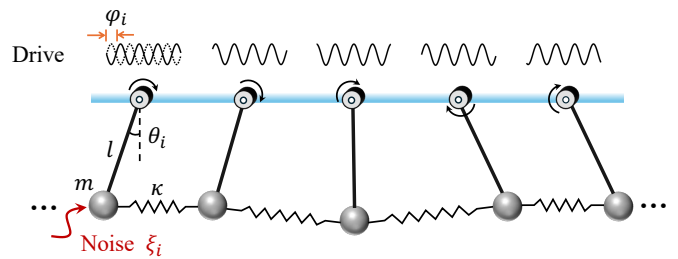


FIG. 1. Illustration of the system of coupled pendulums subject to periodic driving, random disorder, and noise. Physical realization: an array of pendulums, each coupled to its nearest neighbors by springs. The external driving occurs in the torque applied to each pendulum. Disorder is implemented through the random phase (φ_i for the i th pendulum) in the driving, and ξ_i denotes the noise on the i th pendulum.

explored regions. More specifically, we set a goal of synchronization and vary the disorder configuration systematically. A specific configuration generating the desired synchronization represents a satisfactory solution. Otherwise, the search space is expanded until at least one optimal solution is found. Our work demonstrates that the machine-learning approach provides an efficient way to map out the complex relationship between continuous spatial disorder space and synchronization in large-scale dynamical systems, thereby achieving the goal of maximizing synchronization.

We note that similar machine-learning based approaches have been used previously to solve inverse-design problems in other contexts. For example, in material science, rather than exploring the space of material or structural parameter space through iterative refinement, with predefined desired properties, an optimization algorithm was employed to determine the configuration that meets these criteria [34]. This broad machine-learning approach has also been exploited to solve problems such as tracking control of complex dynamical trajectories [35, 36], quantum scattering [37, 38], molecular design [39], and problems in nano-optics [40–42]. Our work extends the utility of inverse design to the realm of collective dynamics in spatial disorder induced synchronization in coupled nonlinear oscillator systems.

In Sec. II, the system of coupled pendulums subject to periodic driving, random disorder, and noise is introduced. In the weakly coupling regime, phase synchronization [43] arises, which can be conveniently characterized by the Shannon entropy index [33]. Section III describes our machine-learning framework for solving the inverse-design problem. Representative results on achieving optimal global phase synchronization are presented in Sec. IV. A discussion is offered in Sec. V. Details about the feedforward neural-network architecture and the optimization algorithm are given in Appendix A. An additional example of inverse design is given in Appendix B.

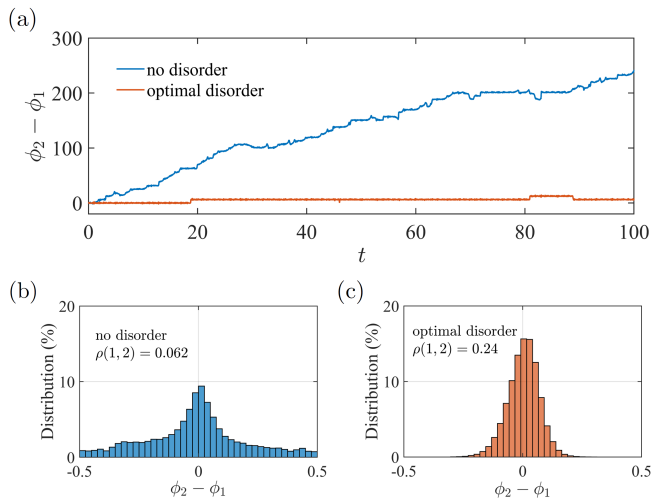


FIG. 2. Phase differences in non-disorder and optimal disorder scenarios. (a) The typical dynamical behavior of the phase difference $\phi_2 - \phi_1$ in a homogeneous system of $N = 24$ pendulums in the absence of disorder, which is effectively a biased random walk (blue). (b) Distribution of the cyclic phase difference $(\phi_2 - \phi_1) \bmod 2\pi$, which is broad. The Shannon entropy index is $\rho(1, 2) = 0.062$, signifying poor phase synchronization. (c) For an optimal disorder configuration (red), the phase difference oscillates about a constant [the orange trace in (b)] and its distribution exhibits a narrow peak. In this case, the Shannon entropy index is $\rho(1, 2) = 0.24$, corresponding to stronger phase synchronization.

II. DISORDERED DRIVEN COUPLED PENDULUM SYSTEM AND PHASE SYNCHRONIZATION

A. System of coupled nonlinear pendulums with disorder

We consider a one-dimensional array of N coupled nonlinear pendulums subjects to noise, as schematically illustrated in Fig. 1, which is described by the following set of coupled differential equations [17, 18, 31]

$$m l^2 \ddot{\theta}_i + \gamma \dot{\theta}_i = -m g l \sin \theta_i + \tau' + \tau \sin(\omega t + \varphi_i) + \kappa(\theta_{i+1} - \theta_{i-1} - 2\theta_i) + \xi_i, \quad (1)$$

for $i = 1, \dots, N$, where θ_i is the angular variable of the i th pendulum, m and l are the mass and length of each pendulum, respectively, g is the gravitational acceleration, γ is the damping coefficient, κ is the coupling parameter between each oscillator with its nearest neighbors, and $\tau' + \tau \sin(\omega t + \varphi_i)$ is the periodic torque that drives the i th pendulum with τ' and τ being constants and ω the driving frequency. The heterogeneity or disorder among the pendulums is manifested as the random phase φ_i in the sinusoidal driving to the i th pendulum. We adopt the parameter values from the previous studies [17, 18, 31]: $m = 1$, $l = 1$, $g = 1$, the damping $\gamma = 0.75$, $\tau' = 0.7155$, $\tau = 0.4$, $\omega = 0.25$, and $\kappa = 0.5$.

The random variable φ_i is taken from a uniform distribution in the interval $[-\pi, \pi]$, where a set of nonidentical driving phases $(\varphi_1, \varphi_2, \dots, \varphi_N)$ introduces the disorder. We use the free boundary condition, i.e., at each end of the array, a fictitious pendulum is introduced: the 0th and the $(N + 1)$ th with $\theta_1 = \theta_0$ and $\theta_N = \theta_{N+1}$. We also assume the presence of noise, which is implemented as the Gaussian white noise term ξ_i in Eq. (1): $\langle \xi_i(t) \xi_j(t') \rangle = D^2 \delta(t - t') \delta_{ij}$ for $i, j = 1, \dots, N$. Note that the noises are not common in the sense that the noise on each pendulum is independent of the noises on the other pendulums. In our simulations, we set $D = 0.05$.

For the noise-free system without the disorder, i.e., $D = 0$ and $\varphi_i = 0$, the motion of each uncoupled individual pendulum is chaotic and the coupled system exhibits spatiotemporal chaos [17]. It was demonstrated that introducing a proper amount of disorder can serve to control or tame spatiotemporal chaos [17, 18, 31]. In addition to the random driving phase [18] in Eq. (1), other forms of disorder have been studied, including random pendulum length [17] and random shortcuts among the pendulums [31], which can induce order and regular spatiotemporal patterns in the system dynamics. Each pendulum displays the periodic spatiotemporal behavior with the same frequency, known as frequency synchronization [44]. In the presence of independent noise, strict frequency-synchronization no longer exists. Instead, phase synchronization [33, 43, 45] becomes crucial, where the instantaneous phase difference between the two pendulums is bounded or approximately constant over time. Phase synchronization can occur even when the coupled pendulums have different frequencies.

B. Instantaneous phase and Shannon entropy index

Our aim is to find some optimal disorder configurations to maximize the phase synchronization. More specifically, the dynamical evolution of each oscillator generates a signal, whose phase can be defined by constructing an analytic signal through the Hilbert transform [43]. In particular, let $\phi_i(t)$ be the instantaneous phase associated with the angular velocity $\dot{\theta}_i(t)$ of the i th pendulum and $\tilde{\theta}_i(t)$ be the Hilbert transform of $\dot{\theta}_i(t)$ given by

$$\tilde{\theta}_i(t) = \frac{1}{\pi} \text{P.V.} \int_{-\infty}^{\infty} \frac{\dot{\theta}_i(\tau)}{t - \tau} d\tau, \quad (2)$$

where P.V. means that the integral is evaluated as a Cauchy principal value. The original signal $\dot{\theta}_i(t)$ and its Hilbert transform $\tilde{\theta}_i(t)$ constitute the following analytic signal [46, 47]

$$\theta_i(t) = \dot{\theta}_i(t) + i \tilde{\theta}_i(t). \quad (3)$$

The instantaneous phase is given by

$$\phi_i(t) = \arctan[\tilde{\theta}_i(t)/\dot{\theta}_i(t)]. \quad (4)$$

In numerical calculations, $\phi_i(t)$ is discretized into a time series constrained to the range $[-\pi, \pi]$, but it should be unwrapped to ensure that $\phi_i(t)$ grows continuously on the entire real line over time. For example, if two adjacent phase values satisfy $|\phi_i(t + \delta t) - \phi_i(t)| > \pi$, where δ is the discrete time step, the latter phase value should be corrected by adding $\text{sgn}[\phi_i(t) - \phi_i(t + \delta t)] \cdot 2\pi$. Noise can cause random phase jumps, hindering the accurate characterization of phase synchronization. An approach is to quantify the deviation of the distribution of the cyclic phase difference $\Phi(i, j)$ between the i th and j th oscillators, defined as [33]

$$\Phi(i, j) = [\phi_i(t) - \phi_j(t)] \bmod 2\pi. \quad (5)$$

In the absence of disorder, the evolution of the relative phase between any two oscillators mimics a biased random walk, as shown in Fig. 2(a). The cyclic phase differences are broadly distributed in the whole range $[-\pi, \pi]$, as shown in Fig. 2(b). For an optimal disorder configuration, the relative phase difference oscillates around a constant, as indicated in Fig. 2(a), suggesting pronounced phase locking with the distribution of the cyclic phase differences significantly different from that in Fig. 2(b). Indeed, in this case, a narrow peak in the distribution appears, as shown in Fig. 2(c).

The Shannon entropy is defined with respect to the distribution of $\Phi(i, j)$ as $S = -\sum_{k=1}^n p_k \ln p_k$, where n is the number of bins used to discretize the distribution, and $S_{\max} = \ln n$. The following Shannon entropy index $\rho(i, j)$ can then be defined [33]

$$\rho(i, j) = \frac{S_{\max} - S}{S_{\max}}. \quad (6)$$

In the absence of any synchronization, the dynamical evolution of the phase difference $\phi_i(t) - \phi_j(t)$ can be viewed as a random walk. In this case, the distribution of $\Phi(i, j)$ is uniform, leading to $\rho(i, j) = 0$. For perfect phase synchronization, the distribution of $\Phi(i, j)$ is a Dirac function, giving $\rho(i, j) = 1$. To characterize the degree of phase synchronization for the whole coupled pendulum system, we average $\rho(i, j)$ over all effective (i, j) pairs to obtain

$$\langle \rho \rangle = \frac{1}{2N(N-1)} \sum_i^N \sum_{j>i}^N \rho(i, j), \quad (7)$$

where pairs with $j \leq i$ are excluded as $\rho(i, j) = \rho(j, i)$ and $\rho(i, i)$ is not meaningful.

For our system of coupled nonlinear pendulums with disorder, a high value of $\langle \rho \rangle$ close to one is generally not attainable. A peculiar property of the Shannon entropy index is that, a low value, e.g., $\langle \rho \rangle = 0.15$, insofar as it is not infinitesimally close to zero, may already correspond relatively strong phase synchronization. In fact, an increase in the $\langle \rho \rangle$ value from, say 0.05 to 0.15, is indicative of the emergence of phase synchronization. However, in the regime of relatively large values of $\langle \rho \rangle$, an increase (e.g., from 0.85 to 0.95) indicates only incremental enhancement in synchronization.

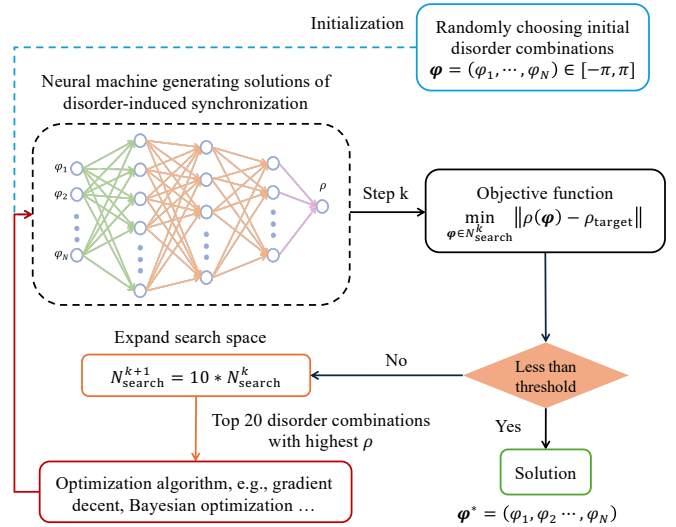


FIG. 3. Flow chart of machine-learning based disorder design to harness synchronization. A feedforward neural network is first trained to accurately predict the Shannon entropy index ρ characterizing the degree of phase synchronization, whose input is the disorder configuration $\varphi = (\varphi_1, \dots, \varphi_N)$. The steps involved in solving the inverse disorder design problem are as follows: (1) randomly choose N_{search}^k disorder configurations $(\varphi_1, \dots, \varphi_N) \in [-\pi, \pi]$ as input to the neural network at step k to obtain the ρ values, one for each disorder configuration, (2) calculate the differences between the N_{search}^k values and the target ρ value, (3) identify the configurations for which the differences in the ρ values are sufficiently small, which are deemed as the solutions, (4) go to the next step $k + 1$ if no solutions are found at step k . At the new step $k + 1$, the search space is expanded by increasing its size to $N_{\text{search}}^{k+1} = 10 * N_{\text{search}}^k$. The top 20 high- ρ disorder configurations are selected as starting points for the fine-tuning inverse design, where local optimization (e.g., gradient descent or Bayesian optimization) is performed in the surrounding parameter space to search for optimal solutions. These steps are repeated until at least one optimal solution φ^* is found.

III. MACHINE LEARNING AND SEARCH-BASED INVERSE DESIGN

For a system of coupled nonlinear oscillators, the mapping from disorder configurations to the strength of phase synchronization can be quite complicated, as the parameter space of disorder configurations grows exponentially with the number of oscillators. Our work is based on the ansatz that this relationship can be captured by a properly designed neural network. In particular, we employ a multilayer feedforward neural network (FNN) to approximate the relationship, as illustrated in Fig. 3. The input layer consists of N neurons that receive the vector defining a disorder configuration: $\varphi = (\varphi_1, \varphi_2, \dots, \varphi_N)$. The input is processed through four hidden layers with [256, 128, 32, 16] neurons, respectively, ultimately generating either the scalar $\langle \rho \rangle$ or an individual value $\rho(i, j)$ at the output layer. This neural network thus contains

six layers L_i , with the layer-to-layer transforms given by

$$L_{i+1} = \text{ReLU}(L_i \cdot \mathbf{W}_i + b_i), \quad i = 1, 2, \dots, 4,$$

where \mathbf{W}_i and b_i represent the weight matrix and bias for the transformation from layer L_i to L_{i+1} , respectively. The activation function is a rectified linear unit (ReLU). For the final (output) layer L_6 , no activation function is applied: $L_6 = L_5 \cdot \mathbf{W}_5 + b_5$, which is simply a linear transform.

The FNN is trained on a large enough volume of ground truth data from solving N stochastic differential equations as in Eq. (1). The collected input data are preprocessed using z -score normalization [48], which removes the mean and scales the data to unit variance. The output data are converted to the unit interval $[0, 1]$ by min-max scaling. The processed dataset is randomly split into a training and a testing set, comprising 80% and 20% of the dataset, respectively. To measure the performance, we use the root mean squared error (RMSE) as the loss function:

$$\mathcal{L}_{\text{RMSE}} = \sqrt{\frac{1}{M} \sum_{i=1}^M (\rho_i - \hat{\rho}_i)^2}, \quad (8)$$

where M is the number of data points, ρ_i and $\hat{\rho}_i$ are real and predicted Shannon entropy indices, respectively. A lower RMSE value corresponds to better performance. In the training process, the weight matrix \mathbf{W}_i and the bias b_i are updated in every epoch, so as to minimize the loss function and improve the performance. In particular, the updates are performed using the adaptive momentum (Adam) optimizer. The specific optimal hyperparameter values are listed in Table I. The construction, training, testing, and predictions of the FNN are accomplished using the open-source packages [49, 50] PYTORCH and SCIKIT-LEARN. More details about FNN and the optimization algorithm are provided in Appendix A.

Once the FNN is well-trained, we generate a search space consisting of N_{search} randomly chosen disorder configurations. Given the desired target value ρ_{target} , the objective function is calculated by

$$o(\varphi) = \min_{\varphi \in N_{\text{search}}} \|\rho(\varphi) - \rho_{\text{target}}\|. \quad (9)$$

If the search space contains sufficiently small objective function values (below a predefined threshold), the corresponding disorder configurations are identified as the

optimal solutions. Otherwise, the process proceeds to the next step: expanding the search space by a factor of 10. Then, the top 20 disorder configurations with the highest ρ are identified. Around each of these configurations, local optimization (e.g., gradient descent or Bayesian optimization) is performed in the surrounding parameter space to search for optimal solutions, as detailed in the caption of Fig. 3. This iterative process continues until at least one optimal disorder configuration φ^* is found. In particular for gradient descent, we update φ based on the calculation of the derivative $\partial o(\varphi)/\partial \varphi$. Since ρ_{target} is fixed, it is only necessary to evaluate the derivative of $\rho(\varphi)$ with respect to φ . For Bayesian optimization, the objective function $o(\varphi)$ is treated as a black-box function. A Gaussian process surrogate model is constructed to approximate $o(\varphi)$, and an acquisition function (such as Expected Improvement) is used to determine the most promising candidate points in the neighborhood of each selected configuration. This probabilistic framework balances exploration and exploitation.

IV. RESULTS

The FNN architecture is trained to predict the strength of local and global phase synchronization under different disorder configurations. Using the well-trained FNN, we search for optimal global phase synchronization over a vast parameter space comprising a sufficiently large number of randomly disordered configurations. The performance is evaluated using both the RMSE and the absolute error. The generalization capability of the FNN will be demonstrated in the high-dimensional disorder parameter space. The results below are for a system of $N = 24$ coupled pendulums. Results for another example, $N = 12$, are given in Appendix B.

A. Machine-learning performance

To simulate the stochastic differential equations, we use the Euler method with the time step $dt = 2\pi/400\omega$. After each time step, the angle variable θ_i is checked and wrapped into the range $[0, 2\pi]$ to ensure consistency with the physical requirement. Given a set of random disordered configurations $(\varphi_1, \varphi_2, \dots, \varphi_N) \in [-\pi, \pi]$, we simulate the dynamical evolution of $\theta_i(t)$ and $\dot{\theta}_i(t)$ over the time period $T = 450$ with random initial conditions $\theta_i(t=0) \in [-\pi/2, \pi/2]$ and $\dot{\theta}_i(t=0) \in [-0.5, 0.5]$. In the early stages of evolution, the system exhibits some transient behaviors, so only the time series $\dot{\theta}_i(50 \leq t \leq 450)$ are used to calculate the Shannon entropy index. All the pairwise indices $\rho(i, j)$ form an $N \times N$ symmetric matrix, where the matrix mean gives $\langle \rho \rangle$. For the same set of disorder configuration, the calculated $\rho(i, j)$ values exhibit fluctuations due to noise, which can be reduced by using the $\rho(i, j)$ and $\langle \rho \rangle$ values for different initial conditions. The average values serve as the ground truth data

TABLE I. Optimal hyperparameter values in FNN

Hyperparameters	Descriptions
$D_{\text{train}} = 80,000$	Size of training set
$D_{\text{test}} = 20,000$	Size of testing set
[256, 128, 32, 16]	Number of neurons in hidden layers
$b_s = 128$	Batch size
epoch = 80	Epoch
$lr = 0.001$	Learning rate

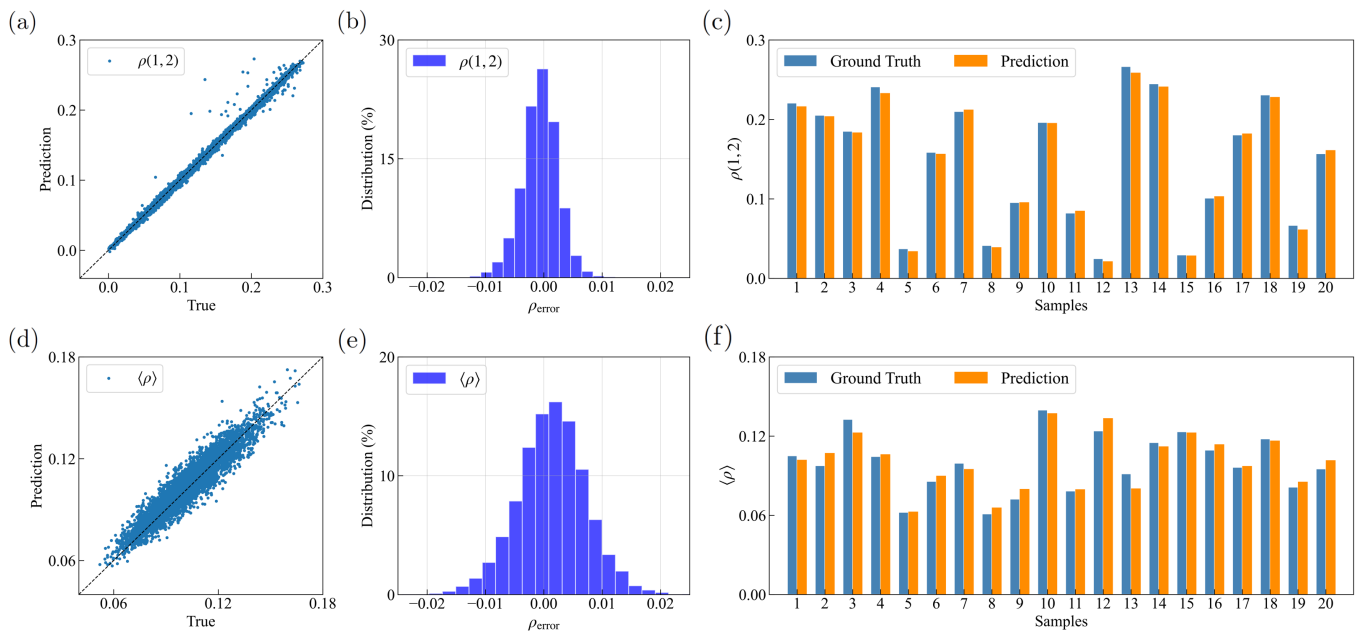


FIG. 4. Performance of proposed feedforward neural network for solving the inverse design problem for synchronization. The system consists of $N = 24$ coupled pendulums. The results in (a-c) are with respect to the pairwise Shannon entropy index $\rho(1, 2)$ for a specific pair of pendulums, while those in (d-f) are for the corresponding average Shannon entropy index $\langle \rho \rangle$. In (a,d), scatter plots of the true versus predicted values are displayed, with 5000 data points randomly selected from the testing set. A heavy concentration of the data points near the diagonal indicates the capability of the trained FNN for predicting phase synchronization. In (b,e), the error distributions of the predictions are shown, which exhibit a near-Gaussian behavior centered at zero. The RMSEs are approximately 0.004 and 0.006, respectively, for $\rho(1, 2)$ and $\langle \rho \rangle$. In (c,f) 20 examples of the disorder configurations with the ground truth (blue) and predicted (orange) values of the Shannon entropy index are shown.

for machine learning. The size of the dataset used for training is 10^5 , and the machine-learning performance is characterized by RMSE. Simulations are run using MATLAB on a desktop computer with 32 CPU cores, 128-GB memory, and one RTX 4000 NVIDIA GPU.

The results for the system of $N = 24$ coupled pendulums are shown in Figs. 4(a-f). In particular, a well trained FNN is capable of predicting the strength of phase synchronization across different disorder configurations. Specifically, we consider the local (for example, the nearest-neighbor) synchronization strength $\rho(1, 2)$ and the global synchronization strength $\langle \rho \rangle$. To evaluate the performance of the FNN, we compare 5000 ground truth values, randomly selected from the testing set, against their corresponding predicted values. The prediction results for $\rho(1, 2)$ and $\langle \rho \rangle$ are presented in Figs. 4(a) and 4(d), respectively, where $\rho(1, 2)$ extends from about 0 to 0.3, and $\langle \rho \rangle$ is relatively lower: spanning from 0.03 to 0.18. In both cases, the predicted values align well with the ground truth along the diagonal dash line, indicating that the FNN effectively captures the global trend. However, some deviations are present, especially in $\langle \rho \rangle$, suggesting room for improvement. Note that $\rho(1, 2)$ is primarily influenced by the disorder parameters φ_1 and φ_2 . In general, the influence of disorder φ_i of i th pendulum on $\rho(1, 2)$ diminishes as their distance from the pendulums 1 and 2 increases. Compared to $\langle \rho \rangle$, $\rho(1, 2)$

has a simpler functional relationship with the disorder configuration, so its FNN prediction is better.

For the entire testing set, the error distributions of predicting $\rho(1, 2)$ and $\langle \rho \rangle$ are shown in Figs. 4(b) and 4(e), respectively, with the absolute error

$$\rho_{\text{error}} = \rho_{\text{true}} - \rho_{\text{pred}}. \quad (10)$$

The RMSEs for $\rho(1, 2)$ and $\langle \rho \rangle$ are approximately 0.004 and 0.006, respectively. Both errors follow a near-Gaussian distribution centered at zero, indicating that the FNN does not introduce systematic bias and maintains a reasonable level of prediction accuracy. Figures 4(c) and 4(f) illustrate 20 sets of predicted (orange) and ground truth (blue) values for $\rho(1, 2)$ and $\langle \rho \rangle$, respectively. Despite deviations, the FNN can still capture the variations and the reasonable agreement suggests that the FNN model generalizes well with respect to different inputs.

It is not surprising that the achievable phase synchronization may depend sensitively on the disorder configuration, but such a high-dimensional functional dependence can be complicated. Nonetheless, with the aid of a well-trained FNN, we can accurately predict the behaviors of the Shannon entropy index in this parameter space. The required time for the prediction process is short and negligible. Figures 5(a-d) present examples of this dependence in some 2D parameter plane in the high-

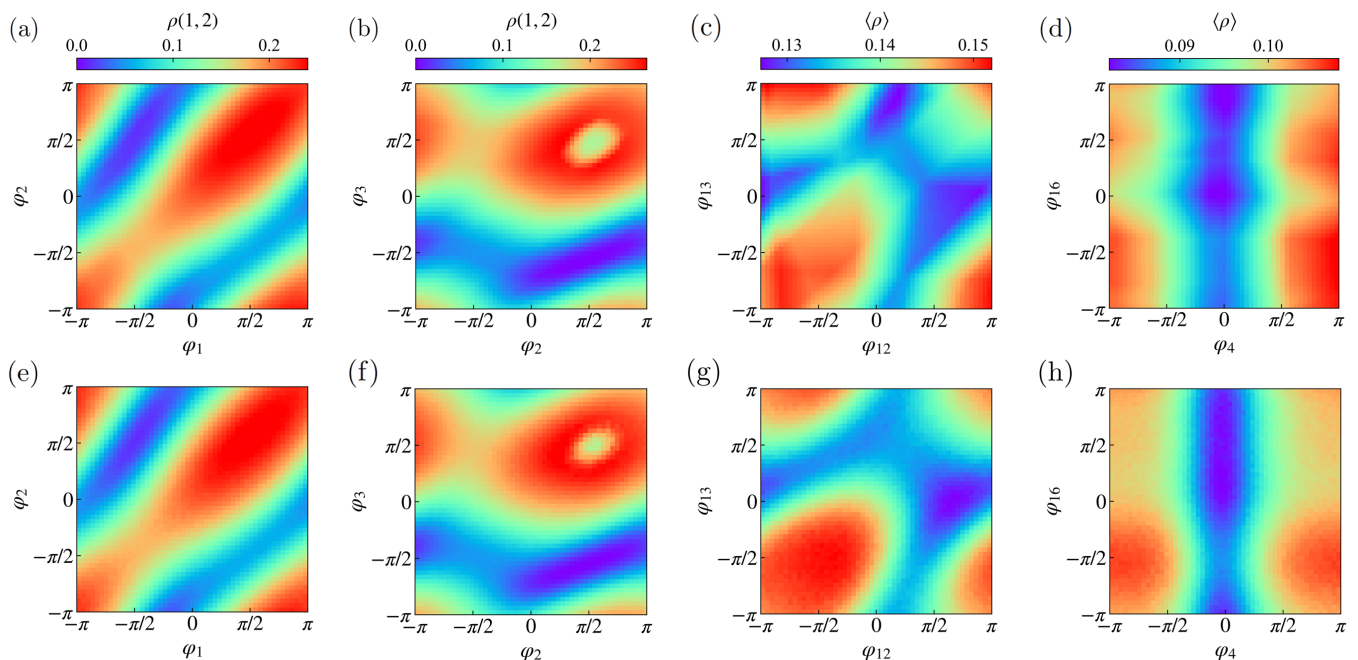


FIG. 5. Ground-truth and FNN predicted values of the pairwise entropy index $\rho(1, 2)$ and average entropy index $\langle \rho \rangle$ on different planes of the disorder parameters. (a,b) Color-coded ground-truth values of $\rho(1, 2)$ in the parameter planes (ϕ_1, ϕ_2) and (ϕ_2, ϕ_3) , respectively. (c,d) Color-coded ground-truth values of $\langle \rho \rangle$ in the parameter planes (ϕ_{12}, ϕ_{13}) and (ϕ_4, ϕ_{16}) , respectively. (e-h) Same as (a-d) but for the FNN predicted values. The agreement between the corresponding panels in the top and bottom rows is indicative of the capability of the FNN for predicting phase synchronization. The system size is $N = 24$.

dimensional space of the disorder parameters, where the values of the entropy index are color-coded. Note that the results in Figs. 5(a-d) are the ground truth, which indeed exhibit a quite sophisticated dependence of the entropy index on the disorder parameters. Figures 5(e-h) show the corresponding FNN-predicted dependence, which closely match the ground truth, accurately capturing the global trends and fine structures of the synchronization landscape. The functional dependence provides insights into how disorder affects synchronization and demonstrate the generalizability of the machine-learning model.

B. Optimal global phase synchronization

For a large system, achieving strong global synchronization, especially with weak coupling strength, is a significant challenge. Introducing disorder and noise provides an effective means to enhance global phase synchronization. Adding noise is not only a practical consideration in experimental settings but also helps mitigate the dynamical sensitivity to initial conditions. On this basis, a carefully selected disorder configuration can generate stable optimal global synchronization [18]. A well-trained FNN model makes it possible to carry out this optimization process in a systematic manner. Figure 6 shows the relationship between the mean RMSE and the dataset size used for training, where the mean RMSEs are cal-

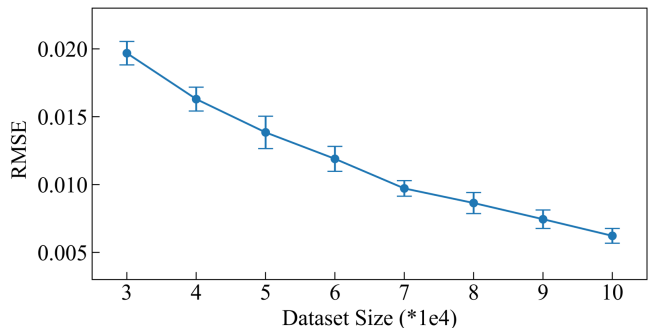


FIG. 6. Effect of Dataset size on RMSE for predicting global phase synchronization as characterized by $\langle \rho \rangle$. The system size is $N = 24$. The mean RMSEs and the error bars (standard deviation) are calculated by training the model five times independently. Increasing the dataset size not only improves the prediction accuracy but also enhances the stability and reliability of the machine-learning model.

culated by training the model five times independently and averaging the results. The mean RMSE decreases as the dataset size increases, allowing one to choose an appropriate dataset size based on the desired prediction accuracy. In addition, the reduced error bar suggests that increasing the dataset size not only improves prediction accuracy (lower mean RMSE) but also enhances the stability and reliability of the trained FNN model.

We search for the optimal global phase synchronization, i.e., making the value of $\langle \rho \rangle^*$ as large as possible, over the high-dimensional parameter space comprising a sufficiently large number N_{search} of randomly disordered configurations. The FNN model replaces both the stochastic differential equation solver and the calculations for $\langle \rho \rangle$, allowing for a computationally efficient search response. Figure 7(a) depicts the values of $\langle \rho \rangle^*$ for different search space sizes N_{search} , where the blue points are obtained by the FNN and corresponding true values are the red points. As N_{search} increases in an exponential manner, initially, $\langle \rho \rangle^*$ increases linearly and tends to be saturated for $N_{\text{search}} = 10^7$. In the subfigure, we illustrate the optimal disorder configuration $(\varphi_1^*, \varphi_2^*, \dots, \varphi_{24}^*)$ with $\langle \rho \rangle^* = 0.219$ for $N_{\text{search}} = 10^7$, where the x -axis represents the ordering of φ_i . Most of φ_i^* values cluster near zero, and only a few of them have the noticeable deviations. Indeed, the disorder configurations φ and $\varphi + c$ produce identical dynamics and the same synchronization strength, where c is an arbitrary constant added to each φ_i . Overall, the optimal strategy is that most of φ_i 's cluster near an arbitrary value with a few deviating from it. In fact, these deviations are crucial: if all φ_i cluster near a single arbitrary value, it would effectively resemble the case of no disorder, generating weak phase synchronization. Figures 7(b) and 7(c) present a visualization of the $N \times N$ matrices with elements $\rho(i, j)$ for two cases: absence of any disorder and optimal disorder, respectively. When there is no disorder, because of the nearest-neighbor coupling, $\rho(i, j)$ is high near the diagonal, indicating relatively strong short-range synchronization. The optimized strategy, by contrast, seeks to strengthen long-range phase synchronization.

V. DISCUSSION

Disorder and noise are typically associated with increased randomness and reduced coherence. However, under appropriate conditions, disorder can enhance synchronization. This work demonstrated, for a system of coupled pendulums under noise, disorder can optimize phase synchronization, making harnessing synchronization possible through the implementation of disorders. A significant challenge is to find the optimal disorder configuration leading to the best possible synchronization. This is particularly so when the system is large, as the parameter space of the disorders is high-dimensional and searching through this space in a brute-force manner is practically infeasible. Machine learning provides a solution.

We have demonstrated that a well-trained FNN can accurately capture the relationship between disorder configurations and phase synchronization strength, allowing computationally efficient prediction over the high-dimensional disorder parameter space. The generalizability of the FNN over the disorder parameter space highlights its potential as a practically usable alternative to

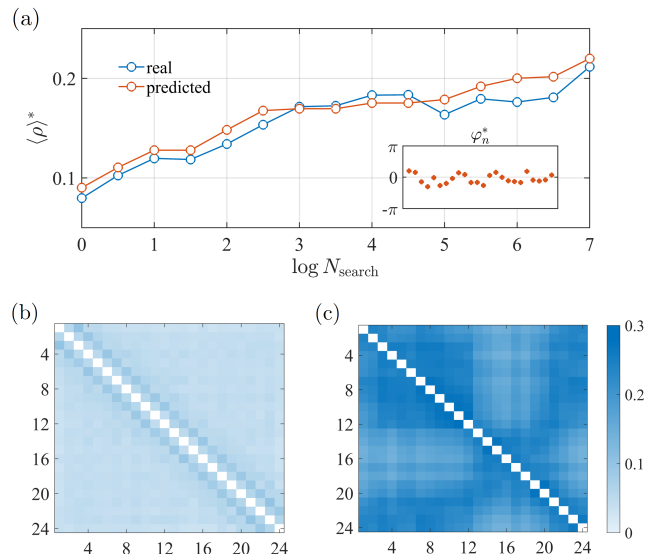


FIG. 7. Example of an optimal disorder configuration. (a) Optimal global phase synchronization for various search space sizes N_{search} . The optimal configuration obtained from $N_{\text{search}} = 10^7$ is illustrated in the subfigure. (b,c) Visualizations of the $N \times N$ matrices with elements $\rho(i, j)$ for the no-disorder case and optimal-disorder configurations, respectively. The diagonal elements are undefined and appear as blank.

traditional numerical solvers. Furthermore, the search-based inverse design successfully identifies optimal disorder configurations that maximize phase synchronization, significantly reducing the computational cost compared to that with brute-force searches. The optimal disorder configurations tend to exhibit specific patterns. It would be interesting to identify and quantify any possible universality of these patterns across different oscillator networks and coupling schemes.

Beyond the specific system studied here, our machine-learning framework can be extended to other nonlinear dynamical systems where disorder and synchronization play a critical role, such as biological rhythms, power grid networks, and laser arrays. The ability to design optimal disorder configurations with machine learning provides an avenue for controlling synchronization in complex systems and opens up possibilities for potential applications in physics, engineering, and beyond.

ACKNOWLEDGMENT

This work was supported by the Office of Naval Research under Grant No. N00014-24-1-2548.

Appendix A: Feedforward neural network

FNN is one of the simplest types of artificial neural networks, with unidirectional information flows from the

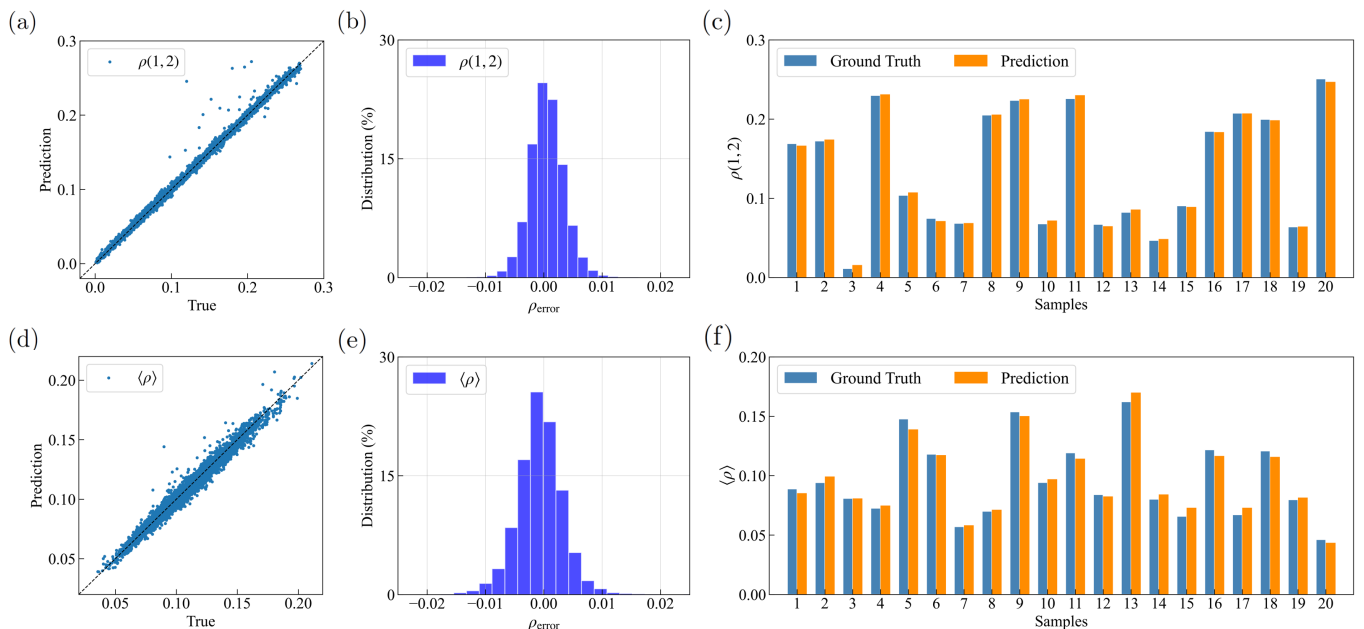


FIG. 8. Prediction performance of the FNN for local and global phase synchronization. The strength of phase synchronization is measured by the Shannon entropy indices $\rho(1, 2)$ in (a-c) and $\langle \rho \rangle$ in (d-f). The system size is $N = 12$. (a,d) Scatter plots of the true versus predicted values, with 5000 data points randomly selected from the testing set. (b,e) Error distributions of the predictions, which exhibit near-Gaussian distributions centered at zero. The RMSEs are approximately 0.004 and 0.004 for $\rho(1, 2)$ and $\langle \rho \rangle$, respectively. (c,f) 20 samples of the ground truth (blue) and predicted (orange) values.

input layer through one or more hidden layers to the output layer [51]. Each layer contains a different number of neurons. The input layer receives the input data, where each neuron represents a distinct feature of the input. There are a number of hidden layers. Each neuron in a hidden layer receives inputs from the neurons in the previous layer, computes a weighted sum of these inputs, and then applies an activation function to the result. The activation functions introduce nonlinearity into the FNN model, where some commonly used functions include ReLU, sigmoid, or tanh. The output layer generates the final output, where the number of neurons depends on the task. The connections between the neurons of two adjacent layers are through the assigned weights. Through updating the weights, a sufficiently large FNN can function as a universal approximator, capable of capturing the complex and underlying relations between input and output.

The core of the FNN's operation lies in the algorithm used to update its weights, often referred to as training. In practice, backpropagation is commonly employed. Each training "epoch" involves a forward pass to compute outputs and a back pass to update the weights. During the forward pass, a loss function is used to quantify the error between the final output and the desired target. Backpropagation then applies the chain rule of calculus to compute the partial derivatives of the loss with respect to each parameter, starting from the output layer and moving backward through the hidden layers. This allows for a gradient-based optimization approach,

typically implemented via algorithms such as stochastic gradient descent (SGD), Adam, or RMSProp. Iterating over multiple epochs, the FNN progressively refines its mapping from inputs to outputs. As an example, Adam (used in this work) is a variant of SGD that adaptively adjusts the learning rate for each parameter, often enhancing both the speed and stability of convergence. For each weight α , the mean m_t and variance v_t of the gradients $g_t = \nabla_{\alpha} \mathcal{L}(\alpha_{t-1})$ are updated at time step t :

$$\begin{aligned} m_t &= \beta_1 m_{t-1} + (1 - \beta_1) g_t, \\ v_t &= \beta_2 v_{t-1} + (1 - \beta_2) g_t^2, \end{aligned} \quad (\text{A1})$$

where β_1 and β_2 are hyperparameters closer to one. A bias correction is then performed: $\hat{m}_t = m_t / (1 - \beta_1^t)$ and $\hat{v}_t = v_t / (1 - \beta_2^t)$. In the end, the weight α_t is updated by

$$\alpha_t = \alpha_{t-1} - \frac{\eta}{\sqrt{\hat{v}_t} + \epsilon} \hat{m}_t, \quad (\text{A2})$$

where ϵ is a small constant added to avoid division by zero, and η is the learning rate.

Appendix B: Results for $N = 12$

We use the same hyperparameter values as those listed in Table I for the FNN to predict the Shannon entropy indices $\rho(1, 2)$ and $\langle \rho \rangle$, except that the number of training epochs is set to 50. Figure 8 shows the performance, where the RMSEs are approximately 0.004 and 0.004 for

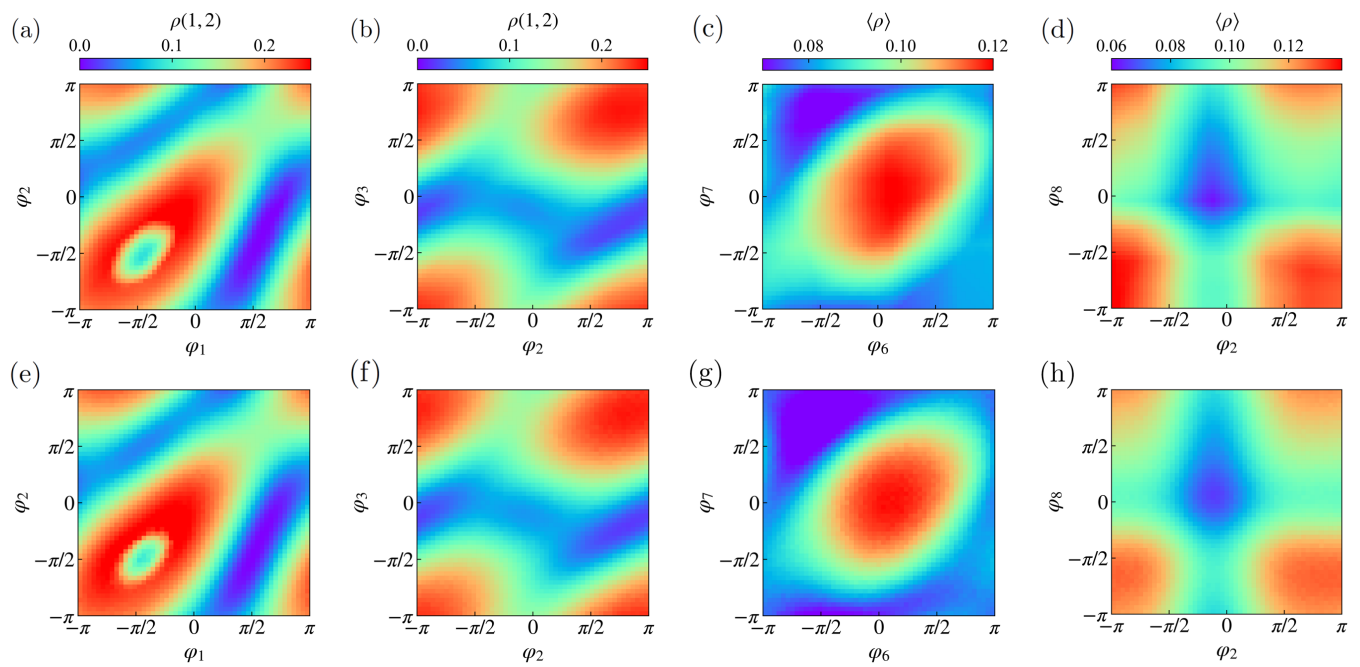


FIG. 9. Ground-truth and FNN predicted values of the pairwise entropy index $\rho(1,2)$ and average entropy index $\langle\rho\rangle$ on different planes of the disorder parameters for system size $N = 12$. The legends are the same as those in Fig. 5.

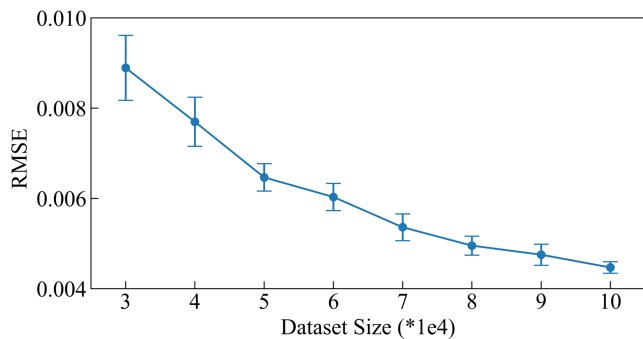


FIG. 10. Effect of Dataset size on RMSE for predicting global phase synchronization. The relevant quantity is the globally averaged entropy index $\langle\rho\rangle$ and the system size is $N = 12$. The mean RMSEs and the error bars (standard deviation) are calculated by training the FNN model five times independently.

$\rho(1,2)$ and $\langle\rho\rangle$, respectively. With the same dataset size of 10^5 , the performance is better than that in the case of $N = 24$, due to a less sophisticated mapping relationship from φ to $\rho(1,2)$ or $\langle\rho\rangle$ for $N = 12$. A less complex mapping reduces the difficulty of function approximation, allowing the FNN to learn more efficiently and achieve higher accuracy with the same amount of training data. The predictions for the color-coded plots of $\rho(1,2)$ and $\langle\rho\rangle$ in the disorder parameter space are shown in Fig. 9, which exhibit somewhat different structures compared to the cases of $N = 24$. This demonstrates the capability of the trained FNN to effectively capture the underlying relationships in the high-dimensional parameter space. The relationship between the mean RMSE and the dataset size used for training is illustrated in Fig. 10.

-
- [1] A. Pikovsky, M. Rosenblum, and J. Kurths, *Synchronization: A Universal Concept in Nonlinear Sciences* (Cambridge University Press, Cambridge, UK, 2001).
 - [2] H. Fujisaka and T. Yamada, Stability theory of synchronized motion in coupled-oscillator systems, *Prog. Theo. Phys.* **69**, 32 (1983).
 - [3] T. Yamada and H. Fujisaka, Stability theory of synchronized motion in coupled-oscillator systems. III: Mapping model for continuous system, *Prog. Theo. Phys.* **72**, 885 (1984).
 - [4] L. M. Pecora and T. L. Carroll, Master stability functions for synchronized coupled systems, *Phys. Rev. Lett.* **80**, 2109 (1998).
 - [5] L. F. Lago-Fernandez, R. Huerta, F. Corbacho, and J. A. Siguenza, Fast response and temporal coherent oscillations in small-world networks, *Phys. Rev. Lett.* **84**, 2758 (2000).
 - [6] P. M. Gade and C.-K. Hu, Synchronous chaos in coupled map lattices with small-world interactions, *Phys. Rev. E* **62**, 6409 (2000).

- [7] J. Jost and M. P. Joy, Spectral properties and synchronization in coupled map lattices, *Phys. Rev. E* **65**, 016201 (2001).
- [8] M. Barahona and L. M. Pecora, Synchronization in small-world systems, *Phys. Rev. Lett.* **89**, 054101 (2002).
- [9] R. Albert, H. Jeong, and A.-L. Barabási, Error and attack tolerance of complex networks, *Nature (London)* **406**, 378 (2000).
- [10] T. Nishikawa, A. Motter, Y.-C. Lai, and F. Hoppensteadt, Heterogeneity in oscillator networks: Are smaller worlds easier to synchronize?, *Phys. Rev. Lett.* **91**, 014101 (2003).
- [11] L. Huang, K. Park, Y.-C. Lai, L. Yang, and K. Yang, Abnormal synchronization in complex clustered networks, *Phys. Rev. Lett.* **97**, 164101 (2006).
- [12] S. Panahi, N. Amaya, I. Klickstein, G. Novello, and F. Sorrentino, Failure of the simultaneous block diagonalization technique applied to complete and cluster synchronization of random networks, *Phys. Rev. E* **105**, 014313 (2022).
- [13] A. Nazerian, J. D. Hart, M. Lodi, and F. Sorrentino, The efficiency of synchronization dynamics and the role of network syncreactivity, *Nat. Commun.* **15**, 9003 (2024).
- [14] J. Chubb, E. Barreto, P. So, and B. j. Gluckman, The breakdown of synchronization in systems of nonidentical chaotic oscillators: Theory and experiment, *Int. J. Bif. Chaos* **11**, 2705 (2001).
- [15] J. Sun, E. M. Bollt, and T. Nishikawa, Constructing generalized synchronization manifolds by manifold equation, *SIAM J. Appl. Dyn. Sys.* **8**, 202 (2009).
- [16] A. Hohl, A. Gavrielides, T. Erneux, and V. Kovanis, Localized synchronization in two coupled nonidentical semiconductor lasers, *Phys. Rev. Lett.* **78**, 4745 (1997).
- [17] Y. Braiman, J. F. Lindner, and W. L. Ditto, Taming spatiotemporal chaos with disorder, *Nature* **378**, 465 (1995).
- [18] S. F. Brandt, B. K. Dellen, and R. Wessel, Synchronization from disordered driving forces in arrays of coupled oscillators, *Phys. Rev. Lett.* **96**, 034104 (2006).
- [19] Y. Zhang and A. E. Motter, Identical synchronization of nonidentical oscillators: when only birds of different feathers flock together, *Nonlinearity* **31**, R1 (2018).
- [20] Y. Zhang, J. L. Ocampo-Espindola, I. Z. Kiss, and A. E. Motter, Random heterogeneity outperforms design in network synchronization, *Proc. Natl. Acad. Sci. (USA)* **118**, e2024299118 (2021).
- [21] Y. Zhang, Y. Sugitani, and A. E. Motter, Synchronizing chaos with imperfections, *Phys. Rev. Lett.* **126**, 164101 (2021).
- [22] A. Nazerian, S. Panahi, and F. Sorrentino, Synchronization in networked systems with large parameter heterogeneity, *Commun. Phys.* **6**, 253 (2023).
- [23] R. Roy and K. S. Thornburg, Experimental synchronization of chaotic lasers, *Phys. Rev. Lett.* **72**, 2009 (1994).
- [24] T. C. Newell, P. M. Alsing, A. Gavrielides, and V. Kovanis, Synchronization of chaotic diode resonators by occasional proportional feedback, *Phys. Rev. Lett.* **72**, 1647 (1994).
- [25] K. Wiesenfeld, P. Colet, and S. H. Strogatz, Synchronization transitions in a disordered Josephson series array, *Phys. Rev. Lett.* **76**, 404 (1996).
- [26] S. Peleš, J. L. Rogers, and K. Wiesenfeld, Robust synchronization in fiber laser arrays, *Phys. Rev. E* **73**, 026212 (2006).
- [27] F. Sorrentino and I. B. Schwartz, Decentralized coupling-when-needed strategy for the synchronization of networked oscillators with delays, *Phys. Rev. E* **111**, 014306 (2025).
- [28] A. G. Vladimirov, G. Kozyreff, and P. Mandel, Synchronization of weakly stable oscillators and semiconductor laser arrays, *Europhys. Lett.* **61**, 613 (2003).
- [29] H. Liu, G. M. Brodnik, J. Zang, D. R. Carlson, J. A. Black, and S. B. Papp, Threshold and laser conversion in nanostructured-resonator parametric oscillators, *Phys. Rev. Lett.* **132**, 023801 (2024).
- [30] N. Nair, K. Hu, M. Berrill, K. Wiesenfeld, and Y. Braiman, Using disorder to overcome disorder: A mechanism for frequency and phase synchronization of diode laser arrays, *Phys. Rev. Lett.* **127**, 173901 (2021).
- [31] F. Qi, Z. Hou, and H. Xin, Ordering chaos by random shortcuts, *Phys. Rev. Lett.* **91**, 064102 (2003).
- [32] O. M. Braun and Y. S. Kivshar, *The Frenkel-Kontorova Model: Concepts, Methods, and Applications*, Vol. 18 (Springer, 2004).
- [33] P. Tass, M. Rosenblum, J. Weule, J. Kurths, A. Pikovsky, J. Volkmann, A. Schnitzler, and H.-J. Freund, Detection of n: m phase locking from noisy data: application to magnetoencephalography, *Phys. Rev. Lett.* **81**, 3291 (1998).
- [34] A. Zunger, Inverse design in search of materials with target functionalities, *Nat. Rev. Chem.* **2**, 0121 (2018).
- [35] Z.-M. Zhai, M. Moradi, L.-W. Kong, B. Glaz, M. Haile, and Y.-C. Lai, Model-free tracking control of complex dynamical trajectories with machine learning, *Nat. commun.* **14**, 5698 (2023).
- [36] Z.-M. Zhai, M. Moradi, B. Glaz, M. Haile, and Y.-C. Lai, Machine-learning parameter tracking with partial state observation, *Phys. Rev. Research* **6**, 013196 (2024).
- [37] C.-D. Han and Y.-C. Lai, Generating extreme quantum scattering in graphene with machine learning, *Phys. Rev. B* **106**, 214307 (2022).
- [38] B. Apagvi, G. Endrédi, and P. Lévy, *Inverse and Algebraic Quantum Scattering Theory: Proceedings of a Conference Held at Lake Balaton, Hungary, 3-7 September 1996*, Vol. 488 (Springer, 2013).
- [39] B. Sanchez-Lengeling and A. Aspuru-Guzik, Inverse molecular design using machine learning: Generative models for matter engineering, *Science* **361**, 360 (2018).
- [40] S. Molesky, Z. Lin, A. Y. Piggott, W. Jin, J. Vucković, and A. W. Rodriguez, Inverse design in nanophotonics, *Nat. Photonics* **12**, 659 (2018).
- [41] S. So, T. Badloe, J. Noh, J. Bravo-Abad, and J. Rho, Deep learning enabled inverse design in nanophotonics, *Nanophotonics* **9**, 1041 (2020).
- [42] Z. Liu, D. Zhu, S. P. Rodrigues, K.-T. Lee, and W. Cai, Generative model for the inverse design of metasurfaces, *Nano Lett.* **18**, 6570 (2018).
- [43] M. G. Rosenblum, A. S. Pikovsky, and J. Kurths, Phase synchronization of chaotic oscillators, *Phys. Rev. Lett.* **76**, 1804 (1996).
- [44] S. Boccaletti, J. Kurths, G. Osipov, D. Valladares, and C. Zhou, The synchronization of chaotic systems, *Phys. Rep.* **366**, 1 (2002).
- [45] Y.-C. Lai, M. G. Frei, I. Osorio, and L. Huang, Characterization of synchrony with applications to epileptic brain signals, *Phys. Rev. Lett.* **98**, 108102 (2007).
- [46] D. Gabor, *J. IEE, London* **93**, 429 (1946).

- [47] P. F. Panter, *Modulation, Noise, and Spectral Analysis: Applied to Information Transmission* (McGraw-Hill, New York, 1965).
- [48] A. Jain, K. Nandakumar, and A. Ross, Score normalization in multimodal biometric systems, *Pat. Recog.* **38**, 2270 (2005).
- [49] A. Paszke, S. Gross, F. Massa, A. Lerer, J. Bradbury, G. Chanan, T. Killeen, Z. Lin, N. Gimelshein, L. Antiga, *et al.*, Pytorch: An imperative style, high-performance deep learning library, *Adv. Neural Inf. Process. Syst.* **32** (2019).
- [50] F. Pedregosa, Scikit-learn: Machine learning in python fabian, *J. Mach. Learn. Res.* **12**, 2825 (2011).
- [51] D. Svozil, V. Kvasnicka, and J. Pospichal, Introduction to multi-layer feed-forward neural networks, *Chemome. Intell. Lab. Sys.* **39**, 43 (1997).